

An experimental and computational study of size-dependent contact-angle of dewetted metal nanodroplets below its melting temperature

Bruno P. Azeredo, Saikumar R. Yeratapally, Josh Kacher, Placid M. Ferreira, and Michael D. Sangid

Citation: [Appl. Phys. Lett.](#) **109**, 213101 (2016); doi: 10.1063/1.4968005

View online: <http://dx.doi.org/10.1063/1.4968005>

View Table of Contents: <http://aip.scitation.org/toc/apl/109/21>

Published by the [American Institute of Physics](#)

An experimental and computational study of size-dependent contact-angle of dewetted metal nanodroplets below its melting temperature

Bruno P. Azeredo,¹ Saikumar R. Yeratapally,² Josh Kacher,^{3,4} Placid M. Ferreira,¹ and Michael D. Sangid^{2,a)}

¹Mechanical Science and Engineering, University of Illinois at Urbana-Champaign, Urbana, Illinois 61801, USA

²School of Aeronautics and Astronautics, Purdue University, West Lafayette, Indiana 47907, USA

³Materials Science and Engineering, University of California Berkeley, Berkeley, California 94720, USA

⁴Materials Science and Engineering, Georgia Institute of Technology, Atlanta, Georgia 30332, USA

(Received 19 August 2016; accepted 6 November 2016; published online 21 November 2016)

Decorating 1D nanostructures (e.g., wires and tubes) with metal nanoparticles serves as a hierarchical approach to integrate the functionalities of metal oxides, semiconductors, and metals. This paper examines a simple and low-temperature approach to self-assembling gold nanoparticles (Au-np)—a common catalytic material—onto silicon nanowires (SiNWs). A conformal ultra-thin film (i.e., <15 nm thick) is deposited onto SiNWs and thermally dewetted, forming nanoparticles in the 6–70 nm range. Two parameters of its morphology are dependent upon dewetting conditions: particle size and particle contact angle. Using transmission electron microscopy imaging, it is found that annealing temperature profile has a strong effect on the particle size. Additionally, the contact angle is found to be dependent on particle size and temperature even below the eutectic temperature of the Au-Si alloy. Molecular dynamics simulations were performed to investigate potential explanations for such experimental observation. In this temperature regime, the simulations reveal the formation of an amorphous phase at the interface between the catalyst and SiNW that is sensitive to temperature. This amorphous layer increases the adhesion energy at the interface and explains the contact angle dependence on temperature. *Published by AIP Publishing.* [<http://dx.doi.org/10.1063/1.4968005>]

Combining the functionalities of zero-dimensional (0D) and one-dimensional (1D) structures opens up a route for integrating the unique properties of nanostructured metals, semiconductors, and oxides. For example, metallic nanoparticles can alone catalyze chemical reactions and support localized surface plasmons. At the same time, high-aspect ratio nanowires offer a large surface area, and unique optical and electrical properties.¹ Together, metal-decorated nanowires exhibit unique properties and find applications in solar energy harvesting,² biomolecular sensing,^{3–5} and cancer cell annihilation.^{6,7} However, the effects of particle shape, spacing, areal density, and size remain largely unaccounted for in literature due to the limitations in particle morphology control during nanoparticle assembly onto 1D nanostructures. There are several methods for self-assembling 0D metal particles onto the surface of semiconducting nanowires: (a) embedded nanocluster formation via rapid thermal chemical vapor deposition,^{7,8} (b) electroless plating nanoparticles,^{3,9} (c) sputtering, (d) thermal evaporation,^{10,11} and (e) atomic layer deposition (ALD).¹² When combining the functionalities of metals and semiconductors, ensuring that the process temperature is below their eutectic point is critical to avoid atomic mixing (via diffusion) and preserve their individual properties. As rapid thermal chemical vapor deposition requires high-temperature processing, all others methods are carried out near RT. Out of a pool of candidates for low-temperature processing, only ALD has been shown to control nanoparticle assembly. As ALD uses costly gas precursors not suitable for large-scale energy applications, alternative methods for the synthesis of 0D metals

onto 1D nanostructures are needed that still provide control over nanoparticle morphology characteristics (i.e., size, density, spacing, shape, and contact angle).

A straight forward and low-cost approach to self-assembling nanoparticles with control over size and density on a surface is thin-film dewetting. In this approach, a metal, dielectric, or polymer solid thin film is heated to approximately one third of its melting temperature, resulting in the film breaking down into nanostructured patterns.¹³ Initially, this breakdown is driven by a competition between the grain boundary grooving and grain growth. Edge retraction later becomes the prevalent mechanism that governs the morphology evolution into the final nanoparticle configuration.¹³ By controlling the film thickness and deposition rate, metal nanoparticles with diameters in the range of 10–400 nm can be assembled with independent control over particle size and area density onto flat substrates like quartz and silicon (Si) wafers.¹⁴ Though much work has been done to understand dewetting onto low aspect ratio nanostructured surfaces (i.e., templated dewetting),^{15,16} dewetting onto high-aspect ratio nanostructures has not been examined in detail.^{16,17}

In addition to thin film dewetting onto high-aspect ratio nanostructures, the control of the particle shape and contact angle during this process is in its nascent form. For example, after the thin film breaks down, gold nanoparticles (Au-np) form a contact angle with the supporting Si surface that is not typically reported as a function of particle size or the annealing temperature profile (i.e., temperature ramp rate and set point temperature).¹⁸ Recent atomistic and experimental studies on the vapor-liquid-solid growth reported on the temperature dependence of the composition of Si rich Au-np for a temperature regime above the eutectic

^{a)}Author to whom correspondence should be addressed. Electronic mail: msangid@purdue.edu

temperature ($T_E = 636$ K) of the Au-Si alloy.^{19,20} In this temperature regime, Si atoms diffuse into the Au lattice to form a superstructure.²⁰ This behavior can modify the cohesive energy of the particle and thus potentially influence the contact angle. Below the eutectic point, it is uncertain if the contact angle should depend on temperature since the alloy system is technically a solid. No experimental or theoretical studies have investigated this fundamental question thus far.

In this paper, we examine the decoration of silicon nanowires (SiNWs) with Au-np by dewetting a uniformly sputtered ultra-thin film (i.e., less than 15 nm). Experimentally, we find that (a) the particle size increases with increasing annealing temperature and (b) the contact angle is proportional to the particle size and inversely proportional to annealing temperature. Computationally, the underlying mechanism for wetting of nanoparticles during dewetting is investigated: the formation of an amorphous layer of intermixed Au and Si atoms at the nanoparticle/substrate interface. This physical effect, observed in Molecular Dynamics (MD) simulations, serves to increase the adhesion energy and explains the temperature-dependence of the contact angle. The statistical data on the particle contact angle were acquired as a function of annealing temperature and particle size using TEM imaging and image analysis and agreed well with our MD model. Understanding how to control nanoparticle assembly onto SiNWs during dewetting may have an impact on harvesting light-matter interactions to the benefit of aforementioned technological applications.

SiNWs were made according to the experimental procedure described in the literature.¹⁴ One large sample of SiNWs was sputtered with Au for 150 s at 40% power in a Denton Desk V employing the all-angle stage rotation feature. Prior to selecting the deposition time, gold films were deposited onto SiNWs at 50 s, 125 s, 150 s, and 200 s and inspected under SEM for continuity. At 150 s and 200 s, the as-deposited film (i.e., no annealing) was continuous. Since sputtered metallic films deposited at room temperature (RT) are typically continuous at about 10 nm thickness, it is estimated that the deposition rate is approximately 0.8 Å/s, and the film thickness ranges from 5 to 15 nm. The sample was cleaved into smaller sizes and later immersed for 60 s in HF (48 wt. %) prior to annealing to remove the native oxide, rinsed with methanol. Samples were placed while still wet inside the annealing chamber, and the chamber was pumped down to $\sim 5 \times 10^{-7}$ Torr. A vacuum level of approximately 10×10^{-2} Torr was achieved within 2 min of sample loading. Once this vacuum level was reached, the temperature was increased to the annealing temperature at a ramp rate of 200 °C/min and held there for 5 h. Annealing time was selected to be an order of magnitude longer than previous studies on^{21,22} ultra-thin films (i.e., less than 15 nm thick), in order to allow it to fully dewet and reach thermodynamic equilibrium. Upon completion of annealing, the chamber was pumped down, and the samples were immersed in methanol. This process occurred within 1 min. After annealing, the samples were stored in methanol to prevent oxidation of the Si substrate.

For TEM sample preparation, the SiNWs were removed from the methanol bath, scraped onto a lacy carbon grid using a clean razor blade, and immediately loaded into the TEM for characterization. Images were taken in a bright-field TEM mode in a JEOL 3010 and using both bright field TEM and high angle

annular dark field (HAADF) scanning (S)TEM imaging in a FEI Titan microscope, both operated at 300 kV. As each grid contained dozens of NWs to image, no tilting of the sample was necessary. Instead, the sample was translated in the x-y plane to locate nanoparticles protruding from the SiNWs, whose axis was approximately perpendicular to the electron beam direction, reducing any projection effects of the nanoparticle contact angles in the micrographs. It is important to note that the contact angle was measured in high-vacuum conditions (i.e., 8.8×10^{-8} Torr), which may alter the contact angle from its configuration in atmospheric conditions. However, since the measurement is performed at RT, the nanoparticles are likely “frozen” in a meta-stable equilibrium due to a lack of sufficient energy, in which to transition to a different configuration.

The contact angle and 2D projected particle area of gold droplets were calculated from TEM and STEM images using a freehand tool in ImageJ analysis package.²³ The particle's cross-section area was measured by approximating them as ellipses in the images. The lengths of the major (2a) and minor (2b) axes were measured for each ellipse and the projected area of the particle was calculated as $A = \pi ab$. The contact angle made by the particle was obtained by averaging the advancing and receding contact angle extracted on either side of the 2D particle image. To reduce the uncertainty produced by a tilted particle, both sides of the Au NP were manually fit with a triangle, and the contact angle was determined by the average value based on the law of cosines for the triangles fitted on either side of the particle. Within each image, a confidence is assigned to the particles based on clarity of the image, visibility of the individual particles, and ease of measurement of the contact angles for individual particles (i.e., nanoparticles perpendicular to the electron beam). The data was only collected from images that were assigned high confidence ratings. Further, very small particles (i.e., whose cross-section area is less than 25 nm²) were not considered in the analysis, to avoid large error in measuring the angle of contact for such small droplets. Overall, 130 high confidence data points were collected, and the data were binned according to the projected area of the particles, at each annealing temperature value. The variation of contact angle with the projected area of the particle was measured at three different temperatures: 323 K, 473 K, and 673 K.

Molecular Dynamics (MD) simulations were conducted to study the dependence of the contact angle on the annealing temperature and Au droplet size. In order to take into consideration the (i) Au-Au pairwise interactions with non-directional bonding within the droplet, (ii) Si-Si pairwise interactions with directional bonding within the substrate, and (iii) Au-Si interactions with mixed metallic-covalent bonding at the interface of the droplet and substrate, a unified angular-dependent embedded atom method (AEAM) interatomic potential was adopted.²⁴ The accuracy of the AEAM potential was validated by comparing the equilibrium lattice constant and cohesive energies of pure Au (with FCC lattice), Si (with diamond cubic lattice), and the cubic lattice superstructures of Au-Si system, including AuSi (with B1 lattice) and Au₃Si (with L1₂ lattice) with the corresponding values obtained from the literature (see Table I). The MD simulations were initialized with the Au droplet (initially as a sphere with diameters ranging from 30 Å to 400 Å) placed on top of a Si

TABLE I. Values for lattice structures of materials.

Lattice Considered	Results from MD simulations		Computational results ²⁴		Experimental (or DFT) results ²⁴		Percentage error (%)	
	a (Å)	E (eV)	a (Å)	E (eV)	a (Å)	E (eV)	a (Å)	E (eV)
Pure Au (FCC)	4.092	−3.93	4.089	−3.93	4.089	−3.93	0.07	0
Pure Si (diamond)	5.413	−4.334	5.431	−4.334	5.431	−4.630	0.3	6.3
Au-Si, B1 crystal lattice	5.362	−3.872	5.362	−3.873	5.28 (DFT)	−3.643 (DFT)	1.55	6.2
Au ₃ Si, L1 ₂ crystal lattice	4.194	−4.033	4.193	−4.035	4.145 (DFT)	−3.149 (DFT)	1.18	27

substrate constrained from any rigid body translation or rotation (as shown in Fig. 2(a)). A sensitivity analysis was conducted on the minimum size of the Si substrate, and no periodic boundary conditions were applied to the system. The atoms in the system were relaxed to find equilibrium using an NVT ensemble. For each droplet specific size, MD simulations were run for 100 ps at a fixed temperature; the simulations were repeated at temperatures of 10 K, 150 K, 323 K, 473 K, and 673 K. The relaxed state of the Au-Si system was used to find the angle of contact between the droplet and substrate via MATLAB's image processing toolbox.

After annealing Au-coated SiNWs at 323, 473, and 673 K, the film fully dewetted into Au-np with diameters in the range of 6–70 nm (Figure 1). It was found that (a) increasing annealing temperature leads to an increase in particle diameter, and (b) the diameter distribution follows a Log-Normal distribution (Figure 1(c)). One possible explanation for the first observation is that there exists a competition in the kinetics of grain growth and grain boundary grooving during morphology evolution in the dewetting process.²⁵ At higher temperatures, the grain growth can precede grain boundary grooving, allowing grains to merge before the break-down transition of the thin film. This effect leads to the formation of larger particles since thin-film grooving is energetically favored at grain boundaries.¹³ At the same time, the second observation—of a Log-Normal distribution—is atypical since dewetting of metallic films onto atomically flat surfaces leads to a normal distribution of particle diameters.^{14,26} Two unique characteristics of the nanowire can affect the particle size distribution: the varying crystal orientation and surface roughness along its circumference. While particles may preferentially form at facets of the nanowire with the lowest energy configuration, dewetted

nanoparticles were observed to form in nanoscopic grooves that spanned along the length of the nanowire (Figure 1(b)). SiNWs manufactured via metal-assisted chemical etching have such groove patterns along their lengths because of edge roughness originally present on the gold patterns used during etching.²⁷ As the etching progresses, the edge roughness profile of the metal catalyst extends through the length of the wire during metal-assisted chemical etching, forming the grooves. These grooves serve as a template for self-assembling nanoparticles and, thus, potentially explain the occurrence of a Log-Normal distribution rather than a normal distribution.

In addition to particle size, the contact angle between dewetted particles and the nanowire surface was examined in detail. Annealed samples were imaged via TEM (Figures 2(c)–2(d)) to resolve the contact angle as a function of particle size and annealing temperature. It was observed that the contact angle increases with (a) an increase in particle size (a trend shown in Fig. 3(a)), and (b) a decrease in temperature. The first observation can be explained based on the size-dependence of cohesive energy for nanoparticles whose size is in the range of 5–30 nm.^{28,29} As the particle size and the number of atoms in it decreases, the particle cohesive energy decreases,^{28,29} leading to smaller contact angles (i.e., wetting). Another possible explanation might include the effect of line tension, which has been argued to influence the size-dependence of the contact angle of nanoscale droplets,^{18,30–32} but the presence of this effect is still debatable at

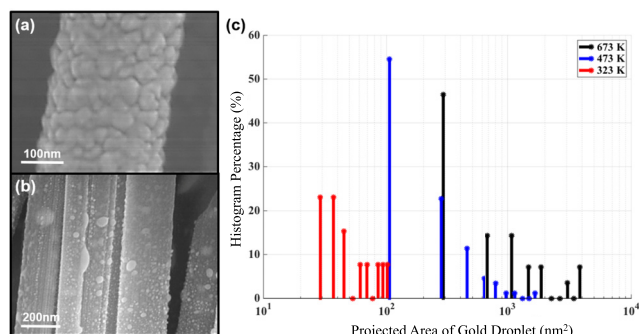


FIG. 1. Dewetting characteristics of Au ultra-thin film onto SiNWs. (a) and (b) are SEM images taken before and after dewetting, respectively, and highlight the assembly of nanoparticles throughout the length of the nanowires. Graph (c) shows the histograms of the particle size distribution along the nanowire as a function of temperature.

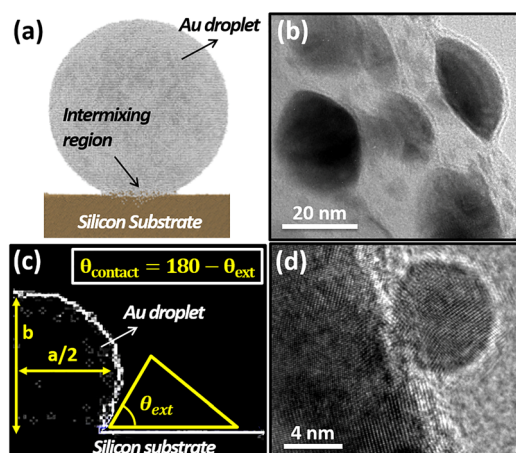


FIG. 2. Molecular dynamics simulation. Image (a) depicts MD simulation result of an Au-np on top of a silicon substrate. Images (b) and (d) are TEM images revealing the crystallinity, size, and contact angle of Au-np onto SiNWs. Image (c) summarizes the image analysis method for obtaining the particle projected area and contact angle. First, the particle shape is outlined via image processing of the TEM data. Next, “a” and “b” are measured and used to compute the projected area of the particle. Finally, θ_{ext} is measured by fitting a triangle near the triple line, and the contact angle is calculated according to formula inset.

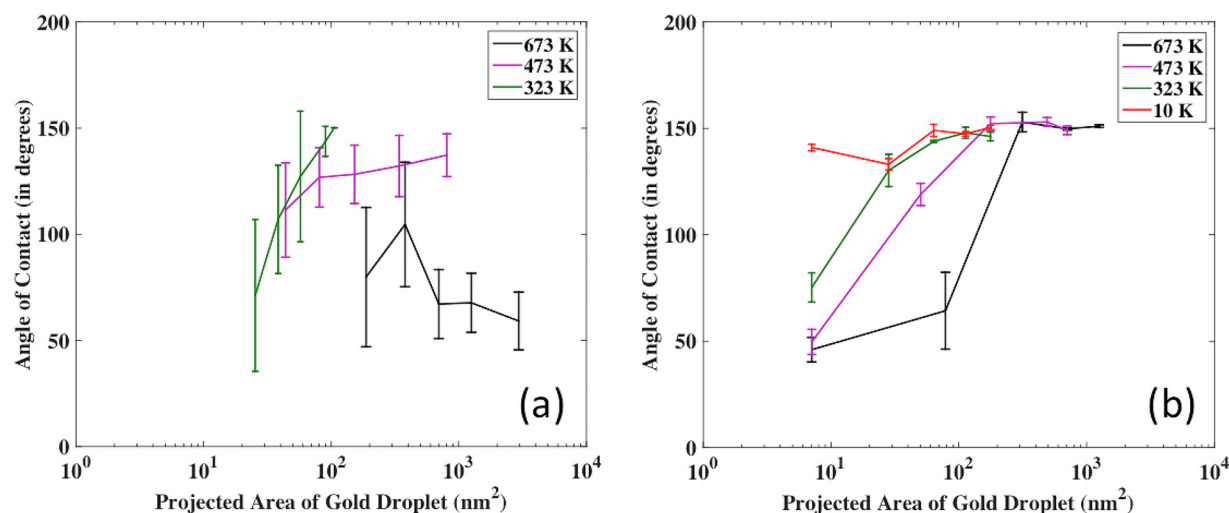


FIG. 3. Contact-angle comparison between experimental and MD simulations results. Left graph (a) depicts experimental results, while right graph (b) depicts computational results for contact angle as a function of particle size and temperature. The error of a single contact angle measurement is 20 degrees. Error bars in part (a) represent 1 standard deviation of a set of measurements for particles sitting on a variety of crystal facets of SiNWs. Trends in temperature and particle size are captured well for temperatures below T_E .

this length scale and not previously investigated for materials below its melting temperature.

To understand the temperature dependence of the contact angle, it is important to consider mechanisms that govern nanoparticle shape evolution during dewetting. First, an increase in temperature activates kinetic processes (i.e., curvature-driven surface diffusion of Au atoms) that drive the film from a metastable (i.e., film) to an equilibrium configuration (i.e., particle).¹³ Simultaneously, a temperature increase can trigger diffusion across the Au-Si interface and, in theory, promote interatomic mixing even below T_E and form an amorphous layer at the Au-Si interface.²⁰ It is hypothesized that this layer exists, and its formation is accelerated as temperature increases, resulting in an increase in the adhesion energy and, consequently, a reduction in the contact angle. Thus, atomic mixing at the interface can explain the temperature dependence of the contact angle below T_E .

In order to further investigate this hypothesis, MD simulations of Au particles onto Si were performed (Fig. 2(a)). It was observed that the contact angle (a) decreases with an increase in annealing temperature for a given particle size, and (b) increases with an increase in particle size. These trends qualitatively match experimental observations (shown in Fig. 3(a)) at temperatures below T_E . In Fig. 3(a), each data point is the average of a set of contact angle measurements made on particles randomly dispersed on the SiNW surface. The large standard deviation in these sets is associated with variations in surface energy intrinsic to different crystallographic facets where particles are located. Single measurement error is 20°. At temperatures above the Au-Si eutectic temperature (636 K), the experimental trend is not captured in the MD simulation (Figure 3). One of the possible reasons for this disagreement is the lack of sufficient time to simulate larger particles which, ultimately, limit atom diffusion across the interface. By limiting the simulation time, the simulation does not capture the formation of a superstructure above T_E , which modifies the mechanism governing the contact angle.²⁰ The error in the prediction trend (above eutectic point) can also be partly attributed to the fact that there is an

8% deviation in eutectic temperature and 13% deviation in eutectic composition of Si predicted by AEAM potential,²⁴ when compared with the experimental phase diagram.

The contact angle dependence on temperature can be related to changes in the adhesion energy due to atomic mixing at the interface. In the post-analysis of the simulation output, the Au-Si interface was examined using a radial distribution function to identify any possible coherence with particular lattice structures (Fig. 4). It was observed that an amorphous region formed between the Au particle and Si substrate as shown in Fig. 2(b). A larger amorphous region was observed at higher temperatures, as expected, due to the increased diffusion kinetics. The amorphous intermixing regions led to larger distances between nearest neighbors in the Si substrate and smaller distances between nearest neighbors in the Au-np. The intermixing region was indeed amorphous, as no obvious superstructure (B1—AuSi or L1₂—Au₃Si was observed in the simulations). Albeit at temperatures above the T_E , the average neighbor distance approached an AuSi superstructure, but in all cases, sufficient strain is present near the interface, thereby affecting the spacing of the lattice structure. For the crystalline constituents (Au—FCC and Si—DC) and superstructure (AuSi—B1), a defect-free lattice structure represents a minimum energy configuration. As the radial distribution function starts to deviate away from these lattice structures, an additional disorder is introduced into the system resulting in an increase in the potential energy of the system. Therefore, as shown by the radial distribution functions, increased temperatures result in more intermixing and an increase in adhesion energy at the interface.

Self-assembly of gold nanoparticles onto high-aspect ratio silicon nanowires has been demonstrated via thin-film dewetting. The resulting morphology of dewetted particles (i.e., size and contact angle) was characterized via TEM imaging. Control over particle size was accomplished by varying the annealing profile, namely, the set-point temperature. Nanoscopic grooves that span the length of the wires serve as a template for dewetting and modify the particle size distribution. Further, the contact angle of gold nanoparticles was determined experimentally as a function of annealing

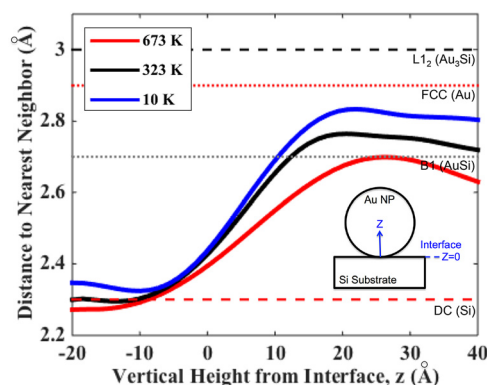


FIG. 4. Radial distribution functions showing average distance to the nearest neighbor as a function of vertical height away from the interface ($Z = 0$ is at the Au-Si interface) and annealing temperature. Equilibrium nearest neighbor distances for different materials are included for reference.

temperature and particle size. It is hypothesized that the formation of an amorphous AuSi layer regulates the temperature dependence of the contact angle. MD simulations were performed to examine this hypothesis. It was found that the simulation agrees with experimental data qualitatively below T_E . This correlation between experiment and simulation is attributed to the formation of an amorphous Au-Si layer at the interface that increases the adhesion energy and, thus, explains the contact angle dependence on temperature.

Many thanks to the Purdue undergraduate research assistants working on analysis of the MD simulations, German Parada, Kevin Vuong, and Konrad Goc. Also, M.D.S. would like to thank Dr. Avinash Dongare for sharing his AEAM potential. B.P.A. and P.M.F. acknowledge financial support for this work from the National Science Foundation (Grant No. 1200780). The work was carried out in part at the Frederick Seitz Materials Research Laboratory Central Facilities at the University of Illinois at Urbana-Champaign. The electron microscopy characterization was done at the Molecular Foundry at Lawrence Berkeley National Laboratory, which is supported by the U.S. Department of Energy under Contract No. DE-AC02-05CH11231. J.K. would also like to thank A. Minor for helpful discussions.

¹V. Schmidt, J. V. Wittemann, S. Senz, and U. Gosele, "Silicon nanowires: A review on aspects of their growth and their electrical properties," *Adv. Mater.* **21**(25–26), 2681 (2009).

²K.-Q. Peng, X. Wang, X.-L. Wu, and S.-T. Lee, "Platinum nanoparticle decorated silicon nanowires for efficient solar energy conversion," *Nano Lett.* **9**(11), 3704–3709 (2009).

³Y. Li, W. Shi, A. Gupta, and N. Chopra, "Morphological evolution of gold nanoparticles on silicon nanowires and their plasmonics," *RSC Adv.* **5**, 49708 (2015).

⁴X. T. Wang, W. S. Shi, G. W. She, L. X. Mu, and S. T. Lee, "High-performance surface-enhanced Raman scattering sensors based on Ag nanoparticles-coated Si nanowire arrays for quantitative detection of pesticides," *Appl. Phys. Lett.* **96**, 053104 (2010).

⁵K. H. Hsu, N. Fang, and K.-H. Fung, "A study on the spectral characteristics of surface enhanced Raman scattering based on far-field extinction and near-field electromagnetic field intensity of 2D nanostructures," *J. Raman Spectrosc.* **46**(1), 59–63 (2015).

⁶Y. Su, X. Wei, F. Peng, Y. Zhong, Y. Lu, S. Su, T. Xu, S.-T. Lee, and Y. He, "Gold nanoparticles-decorated silicon nanowires as highly efficient near-infrared hyperthermia agents for cancer cells destruction," *Nano Lett.* **12**(4), 1845–1850 (2012).

⁷G.-S. Park, H. Kwon, D. W. Kwak, S. Y. Park, M. Kim, J.-H. Lee, H. Han, S. Heo, X. S. Li, J. H. Lee, Y. H. Kim, J.-G. Lee, W. Yang, H. Y. Cho,

S. K. Kim, and K. Kim, "Full surface embedding of gold clusters on silicon nanowires for efficient capture and photothermal therapy of circulating tumor cells," *Nano Lett.* **12**(3), 1638–1642 (2012).

⁸M. I. den Hertog, J.-L. Rouviere, F. Dhalluin, P. J. Desré, P. Gentile, P. Ferret, F. Oehler, and T. Baron, "Control of gold surface diffusion on silicon nanowires," *Nano Lett.* **8**(5), 1544–1550 (2008).

⁹Z. Peng, H. Hu, M. I. B. Utama, L. M. Wong, K. Ghosh, R. Chen, S. Wang, Z. Shen, and Q. Xiong, "Heteroepitaxial decoration of Ag nanoparticles on Si nanowires: A case study on Raman scattering and mapping," *Nano Lett.* **10**(10), 3940–3947 (2010).

¹⁰L. Cao, B. Garipcan, E. M. Gallo, S. S. Nonnenmann, B. Nabet, and J. E. Spanier, "Excitation of local field enhancement on silicon nanowires," *Nano Lett.* **8**(2), 601–605 (2008).

¹¹H. K. Yu and J.-L. Lee, "Growth mechanism of metal-oxide nanowires synthesized by electron beam evaporation: A self-catalytic vapor-liquid-solid process," *Sci. Rep.* **4**, 6589 (2014).

¹²N. P. Dasgupta, C. Liu, S. Andrews, F. B. Prinz, and P. Yang, "Atomic layer deposition of platinum catalysts on nanowire surfaces," *J. Am. Chem. Soc.* **135**(35), 12932–12935 (2013).

¹³C. V. Thompson, "Solid-state dewetting of thin films," *Annual Review of Materials Research* **42**, 399–434 (2012).

¹⁴B. P. Azeredo, J. Sadhu, J. Ma, K. Jacobs, J. Kim, K. Lee, J. H. Eraker, X. Li, S. Sinha, N. Fang, P. Ferreira, and K. Hsu, "Silicon nanowires with controlled sidewall profile and roughness fabricated by thin-film dewetting and metal-assisted chemical etching," *Nanotechnology* **24**(22), 225305 (2013).

¹⁵Y. M. Wang, L. Lu, B. M. Srinivasan, M. Asbahi, Y. W. Zhang, and Joel K. W. Yang, "High aspect ratio 10-nm-scale nanoaperture arrays with template-guided metal dewetting," *Sci. Rep.* **5**, 9654 (2015).

¹⁶J. Ye and C. V. Thompson, "Templated solid-state dewetting to controllably produce complex patterns," *Adv. Mater.* **23**(13), 1567–1571 (2011).

¹⁷Y.-J. Oh, J.-H. Kim, C. V. Thompson, and C. A. Ross, "Templated assembly of Co-Pt nanoparticles via thermal and laser-induced dewetting of bilayer metal films," *Nanoscale* **5**, 401–407 (2013).

¹⁸A. Checco, P. Guenoun, and J. Daillant, "Nonlinear dependence of the contact angle of nanodroplets on contact line curvature," *Phys. Rev. Lett.* **91**(18), 186101 (2003).

¹⁹H. Wang, L. A. Zepeda-Ruiz, G. H. Gilmer, and M. Upmanyu, "Atomistics of vapour-liquid-solid nanowire growth," *Nat. Commun.* **4**, 1956 (2013).

²⁰T. U. Schüllli, R. Daudin, G. Renaud, A. Vaysset, O. Geaymond, and A. Pasturel, "Substrate-enhanced supercooling in AuSi eutectic droplets," *Nature* **464**, 1174 (2010).

²¹J. Mizsei, and V. Lantto, "In situ AFM, XRD and resistivity studies of the agglomeration of sputtered silver nanolayers," *J. Nanopart. Res.* **3**, 271–278 (2001).

²²H. C. Kim, T. L. Alford, and D. R. Allee, "Thickness dependence on the thermal stability of silver thin films," *Appl. Phys. Lett.* **81**(22), 4287 (2002).

²³See <http://imagej.nih.gov> for ImageJ software tools.

²⁴A. M. Dongare, M. Neurock, and L. V. Zhigilei, "Angular-dependent embedded atom method potential for atomistic simulations of metal-covalent systems," *Phys. Rev. B* **80**, 184106 (2009).

²⁵E. J. Luber, B. C. Olsen, C. Ophus, and D. Mitlin, "Solid-state dewetting mechanisms of ultrathin Ni films revealed by combining in situ time resolved differential reflectometry monitoring and atomic force microscopy," *Phys. Rev. B* **82**, 085407 (2010).

²⁶T. W. H. Oates and H. Sugime, "Combinatorial surface-enhanced Raman spectroscopy and spectroscopic ellipsometry of silver island films," *J. Phys. Chem. C* **113**, 4820–4828 (2009).

²⁷M. G. Ghossoub, K. V. Valavala, M. Seong, B. Azeredo, K. Hsu, J. S. Sadhu, P. K. Singh, and S. Sinha, "Spectral phonon scattering from sub-10 nm surface roughness wavelengths in metal-assisted chemically etched Si nanowires," *Nanoletters* **13**, 1564–1571 (2013).

²⁸R. Kumar and M. Kumar, "Effect of size on cohesive energy, melting temperature and Debye temperature of nanomaterials," *Ind. J. Pure Appl. Phys.* **50**, 329–334 (2012).

²⁹Q. Jiang, J. C. Li, and B. Q. Chi, "Size-dependent cohesive energy of nanocrystals," *Chem. Phys. Lett.* **366**(5–6), 551–554 (2002).

³⁰A. Checco, H. Schollmeyer, J. Daillant, P. Guenoun, and R. Boukherroub, "Nanoscale wettability of self-assembled monolayers investigated by non-contact atomic force microscopy," *Langmuir* **22**, 116–126 (2006).

³¹A. Méndez-Vilas, A. B. Jódar-Reyes, and M. L. González-Martín, "Ultrasmall liquid droplets on solid surfaces: production, imaging, and relevance for current wetting research," *Small* **5**(12), 1366–1390 (2009).

³²J. H. Weijs, A. Marchand, B. Andreotti, D. Lohse, and J. H. Snoeijer, "Origin of line tension for a Lennard-Jones nanodroplet," *Phys. Fluids* **23**(2), 022001 (2011).